ACS APPLIED MATERIALS & INTERFACES

Research Article

www.acsami.org

Modulation of Electronic and Self-Assembly Properties of a Donor–Acceptor–Donor-Based Molecular Materials via Atomistic Approach

Joydeep Dhar,[†] K. Swathi,[‡] Durga Prasad Karothu,[†] K. S. Narayan,[‡] and Satish Patil*,[†]

[†]Solid State and Structural Chemistry Unit, Indian Institute of Science, Bangalore 560012, India

[‡]Chemistry and Physics of Materials Unit, Jawaharlal Nehru Centre for Advanced Scientific Research, Jakkur, Bangalore 560064, India

Supporting Information

ABSTRACT: The performance of molecular materials in optoelectronic devices critically depends upon their electronic properties and solid-state structure. In this report, we have synthesized sulfur and selenium based (**T4BT** and **T4BSe**) donor–acceptor–donor (D–A–D) organic derivatives in order to understand the structure–property correlation in organic semiconductors by selectively tuning the chalcogen atom. The photophysical properties exhibit a significant alteration upon varying a single atom in the molecular structure. A joint theoretical and experimental investigation suggests that replacing sulfur with selenium significantly reduces the band gap and molar absorption coefficient because of lower electronegativity and ionization potential of selenium. Single-crystal X-ray diffraction analysis showed differences in their solid-state packing and intermolecular interactions. Subsequently, difference in the solid-state packing results variation in self-assembly. Micorstructural changes within these materials are correlated to their electrical resistance variation, investigated by conducting probe atomic force microscopy (**CP-AFM**) measurements. These results provide useful guidelines to understand the fundamental properties of D–A–D materials prepared by atomistic modulation.

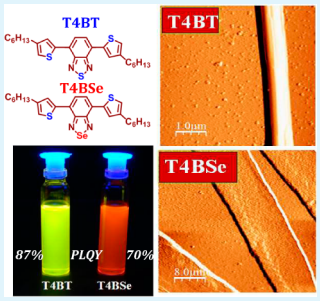

KEYWORDS: *selenium, electronic property, self-assembly, microstructure, conductivity*

1. INTRODUCTION

π-Conjugated organic materials are promising candidates for next-generation optoelectronic devices.[1,2] The main advantages of organic over the silicon-based devices are flexibility, roll-to-roll processing, and cost-effective device fabrication.[3] Diverse synthetic possibilities and manipulative structure-dependent electronic properties have encouraged researchers to explore the horizons in material design and synthesis.[4−6] Subsequently, the integration of these materials in optoelectronic devices has laid the cornerstone for fundamental understanding of structure–property relationship to develop high-performance materials for optoelectronic applications.[7,8] The performance of organic semiconductors in electronic devices is primarily restricted by moderate charge-carrier mobilities as compared to their inorganic counterparts,[4,9] though such a bottleneck in recent years has greatly been overcome by rational material design and synthesis,[10−12] foreshowing bright prospects. The charge-transport property of organic semiconductors is limited by the weak molecular organization and absence of long-range macroscopic order, essential to drive the charges with minimal barriers and scattering.[9] To surmount these drawbacks, control at nanoscale morphologies has paramount importance in the bottom-up fabrication of devices based on organic semiconductors.[13−15] Supramolecular self-assembly with a variety of weak intermolecular interactions enhances the electronic coupling among neighboring molecules leading to the decrease in trap-states.[16,17] Because the transport in organic semiconductors generally follows hopping of charge carriers among the localized centers,[18] a one-dimensional (1D) self-organization of organic molecules along the direction of charge transport (π–π stacking) is presumed to provide the channel for charges to migrate with a minimum energetic barrier.[19] Such anisotropic transport along the 1D nanostructure has demonstrated to improve the charge carrier mobilities in contrast to the bulk or thin film.[20]

In recent years, a lot of emphasis has been given to elucidate the role of the heteroatom, mainly the influence of the chalcogen atom in governing the electronic properties and solid-state packing of organic semiconductors.[21,22] Optimized energy levels with favorable intermolecular interactions have contributed to the superior device performance and in particular thiophene and its derivatives have shown considerable interest.[23] Recently, selenophene-based functional materials have exhibited superior properties.[11,24−27] Theoretical analysis has predicted selenium-containing molecules to have advantages over their sulfur-based counterparts because of their suitable electronic structures.[28,29] Moreover, stronger intermolecular interactions in selenophene derivatives exhibit favorable nanomorphologies, which in general have showed enhanced charge transport.[22,30] Of late, atomistic approach in determining the fundamental structure-property correlation in chalcogen derivatives has attracted a lot of attention to fine-tune the electronic and structural properties because these directly influence the solid-state packing and hence, the

Received: October 8, 2014
Accepted: December 9, 2014
Published: December 22, 2014

Scheme 1. Synthesis of T4BT and T4BSe

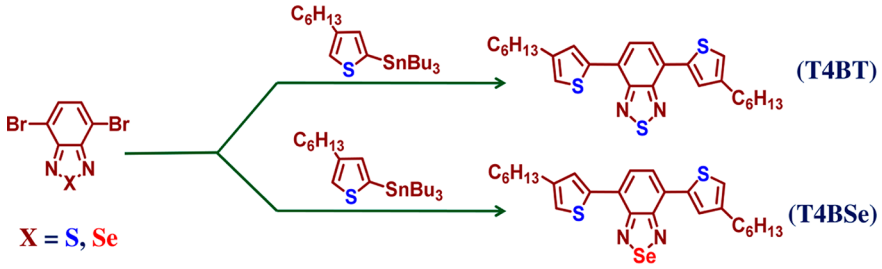

transport characteristic of the organic semiconductors.[21,25,31,32] As a result, the evaluation of charge transport has become one of the effective ways to establish the structure dependent molecular properties in organic semiconductors. Functional materials comprising of molecular semiconductors are the ideal choice to investigate such correlations as subtle variations in molecular architecture reflect distinctive alterations in their functionalities.[33] Hence, molecular materials with higher purity and definitive structural integrity have opened up the real possibility to ascertain structure−property correlation in organic semiconductors and in this respect, small molecule with donor−acceptor−donor (D−A−D) structure confers the ideal platform to realize the changes in the property bestowed due to structural manipulation.[34] D−A−D structure with electron-donating and electron-accepting groups reduces the band gap by the newly formed high-lying HOMO and low-lying LUMO as compared to their corresponding individual donor and acceptor moieties.[35] Because molecular orbitals are generated by mixing of atomic orbitals, variation of a single atom, either in the donor or acceptor unit, clearly reflects on its electronic properties.[36] Therefore, the atomistic influence of a chalcogen element on charge transport can be perceived in a molecular semiconductor with D−A−D backbone. However, it should be mentioned that the chalcogen atom replacement can have cascading, unintended effects in the bulk film form where the transport properties need not necessarily reflect the electronic structure, but are also governed by microstructure and geometrical factors.

Here in our study, we have synthesized thiophene coupled 2,1,3-benzothiadiazole (**T4BT**) and its selenium analog (**T4BSe**) D−A−D molecules and studied their photophysical and electrical properties to investigate the effect of selenium substitution in the acceptor moiety. These two molecular semiconductors quite distinctly and spontaneously self-assemble from common organic solvents and such self-organization was utilized to evaluate the electrical conductivity to apprehend the role of the chalcogen atom in governing the molecular properties.

2. EXPERIMENTAL SECTION

2.1. Materials. 3-Bromothiophene, Ni(dppp)Cl_2, *n*-butyllithium, and *n*-tributyltin chloride were received from Sigma-Aldrich. Triethylamine, *o*-phenylenediamine, thionyl chloride, hydrobromic acid (HBr), bromine, sodium sulfate (Na_2SO_4), toluene, dimethylformamide (DMF), dimethyl sulfoxide (DMSO), diethyl ether, dichloromethane (DCM), chloroform, hexane, and ethyl acetate of analytical grade were purchased from SD. Fine chemicals. Sodium borohydride ($NaBH_4$), cobalt chloride ($CoCl_2$), ethanol, and 1-bromohexane were supplied by Spectrochem. All the chemicals were used as received without any further purification.

2.2. Synthesis. Two molecules, 4,7-bis(3′-hexylthiophen-2-yl)-2,1,3-benzothiadiazole (**T4BT**) and 4,7-bis(3′-hexylthiophen-2-yl)-2,1,3-benzoselenadiazole (**T4BSe**), were synthesized by Stille coupling reaction between 4-hexyl-2-tributylstannylthiophene and 4,7-dibromo-2,1,3-benzochalcogenadiazole as reported in the literature.[37−42] 4-Hexyl-2-tributylstannylthiophene was synthesized from 4-hexylthiophene following Grignard reaction. On the other side, 4,7-dibromo-2,1,3-benzochalcogenadiazole was synthesized following a multistep reaction scheme. Synthetic procedures with ^1H and ^{13}C NMR spectra of **T4BT** and **T4BSe** have been provided in the Supporting Information.

2.3. Characterization. The ^1H and ^{13}C NMR spectra were recorded on Bruker Avance NMR spectrometer using $CDCl_3$ and TMS as solvent and internal standard, respectively. The optical absorption spectra of two chalcogen derivatives were collected in six different solvents; toluene, chloroform, DCM, ethanol, DMF, and DMSO on PerkinElmer (Lambda 35) spectrometer at room temperature. Steady state fluorescence spectra of **T4BT** and **T4BSe** were monitored in Horiba JobinYvon Fluorolog3 fluorometer and fluorescence quantum yield was determined using integrated sphere attached as an additional accessory to the fluorometer. Time-resolved fluorescence decay measurements were carried out by time-correlated single photon counting (TCSPC) method with picosecond laser (469 nm, 25 ps). Field-emission scanning electron microscopy (FESEM) images were collected in the Ultra 55, Zeiss electron microscope at 5 kV at room temperature. Atomic force microscopy (AFM) images were recorded in tapping mode on Dimension ICON from Bruker Corporation. Single-crystal X-ray diffraction data was collected on an Oxford Xcalibur (Mova) diffractometer equipped with an EOS CCD detector with Mo Kα radiation (λ = 0.71073 Å). The temperature was maintained at 110 K during data collection using the cryojet-HT controller. Differential scanning calorimetry (DSC) analysis was performed in Mettler Toledo DSC1 STARe system with N_2 flow of 40 mL/min at a heating and cooling rate of 5 °C/min with an empty Al pan taken as standard. Thermogravimetric analysis (TGA) was carried out in Mettler Toledo TGA SDTA 851 instrument at a heating rate of 10 °C/min under a nitrogen atmosphere. Redox properties of the two molecules were evaluated by cyclic voltammetry (CH instrument). Ag/AgCl was used as a reference electrode, whereas platinum (Pt) disk and wire were employed for working and counter electrodes, respectively. Dry chloroform and 0.1 M tetrabutylammonium hexafluorophosphate were used as solvent and supporting electrolyte. Ferrocene/ferrocenium (Fc/Fc^+) couple was used as standard electrochemical reference. The energies of highest occupied molecular orbital (HOMO) and lowest unoccupied molecular orbital (LUMO) were calculated from the respective oxidation and reduction potential. At the experimental condition, ferrocene oxidizes to ferrocenium ion at 0.4 V with respect to Ag/AgCl system, the position of HOMO and LUMO were computed from eq 1 and the electrochemical band gap was determined from the difference between them.

$$\text{HOMO} = -(E_{ox} + 4.4)\ \text{eV};\ \ \text{LUMO} = -(E_{red} + 4.4)\ \text{eV} \quad (1)$$

Electrical transport with nanometer resolution was probed by conducting probe-AFM (CP-AFM), which provides a direct correlation of conductivity with topographical features of an organic semiconductor. The sample was drop casted from a 10 mg/mL solution of 1,2-dichlorobenzene onto Cr-gold coated glass coverslips (5 nm Cr/50 nm gold coated by physical vapor deposition at 1×10^{-6}

dx.doi.org/10.1021/am506905b | ACS Appl. Mater. Interfaces 2015, 7, 670−681

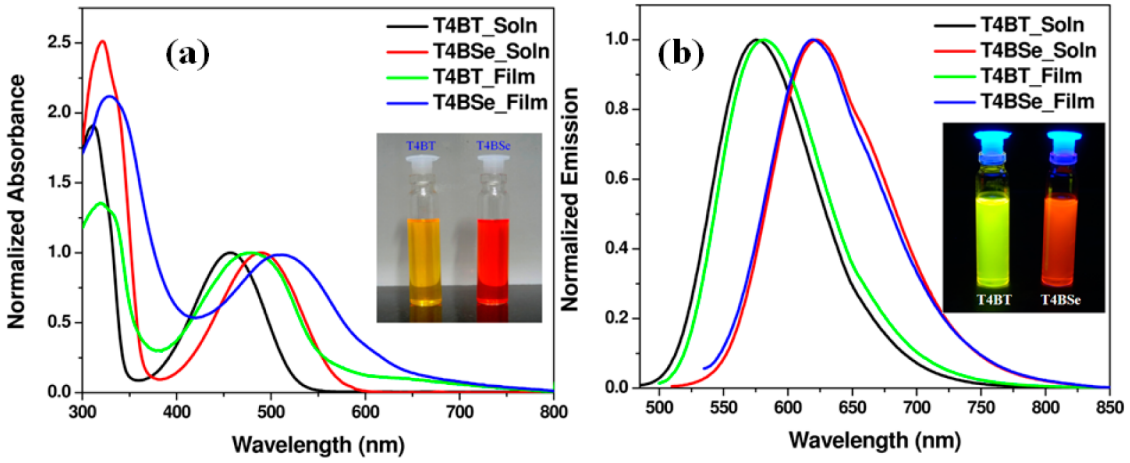

Figure 1. (a) Absorption and (b) emission spectra of **T4BT** and **T4BSe** in chloroform solution and thin film. Inset shows the photographs of **T4BT** and **T4BSe** under (a) white light and (b) UV light (~365 nm).

Table 1. Summary of Optical, Electrochemical, and Theoretical Data for T4BT and T4BSe

	optical properties						electrochemical properties[a]			DFT[b]
compds	λ_{abs}(max) (nm)	ε_{max} ($M^{-1}cm^{-1}$)	λ_{em}(max) (nm)	PLQY (%) soln	Stokes shift (eV)	E_g^{Opt} (eV)	HOMO (eV)	LUMO (eV)	E_g^{elec} (eV)	E_g^{theo}
T4BT	445	14640	575	87	0.63	2.29	−5.55	−3.27	2.28	2.69
T4BSe	491	6560	622	70	0.53	2.13	−5.49	−3.39	2.10	2.55

[a]The data calculated from cyclic voltammetry experiments with reference to the Ag/AgCl electrode and ferrocene/ferrocenium (Fc/Fc^+) couple as standard. [b]The values obtained from the difference between the HOMO and LUMO energy levels optimized at the B3LYP/6-31g(d) basis set.

mbar base pressure). Although the underlying gold acts as one electrode, a conducting cantilever (ElecrtiCont-G from Budget Sensors) coated with chrome-platinum with a tip size less than 25 nm was used as the other electrode for $I(x)$ measurements. The experimental setup for CP-AFM is shown in Figure S5 (Supporting Information). The cantilever is connected to a circuit board on the head of a JPK nanowizard III atomic force microscope. A stable DC bias in the range −10 to 10 V can be applied to gold and the resulting current flowing through the self-assembled semiconducting molecules into the cantilever tip in contact mode is obtained along with its corresponding topographic image.

3. RESULTS AND DISCUSSION

Two D−A−D derivatives, **T4BT** and **T4BSe** (Scheme 1) were prepared by Stille coupling between 4-hexyl-2-tributylstannylthiophene and 4,7-dibromo-2,1,3-benzochalcogenadiazole. The purity of the compounds was confirmed by ^1H, ^{13}C NMR, and ESI-mass spectroscopy (see the Supporting Information).

3.1. Optical Properties. Significant changes were observed in the optical properties with a single atom variation in **T4BT** and **T4BSe** reflecting the substantial contribution of the chalcogen atom on the electronic properties. UV−visible absorption and fluorescence spectra of **T4BT** and **T4BSe** in solution and solid state are shown in Figure 1a, b, respectively. The donor−acceptor property of these molecules is exhibited in their characteristic dual-band absorption spectra where the high energy band attributes to the $\pi \rightarrow \pi^*$ transition. In addition, the low energy band indicates an intramolecular charge transfer transition. For both molecules, because of close packing and aggregation, these two bands show a bathochromic shift in the thin film as compared to the solution. For **T4BT**, peaks at 310 and 445 nm in chloroform shifted to 319 and 480 nm in thin film, respectively. Similarly, in the case of the selenium analog (**T4BSe**), those two peaks were shifted to 329 and 510 nm in solid state from 322 and 491 nm in chloroform solution. In both the molecules, greater red shift was observed for the low energy band in comparison with the high energy band and in the thin film, the intensity of the charge transfer band is enhanced as compared to the $\pi \rightarrow \pi^*$ bands. Especially for **T4BT** molecules, we always observe a broad tail in the charge transfer band in the thin film absorption spectrum indicating the presence of a higher degree of aggregation. Higher red shift with concomitant enhancement of the low energy transition suggests that the intermolecular charge transfer also simultaneously plays a crucial role in the optical properties of the thin film and the peak intensity is enhanced because of strong interaction in the solid state.[21] As we move from **T4BT** to **T4BSe**, the significant red shift in the charge transfer band by 47 nm in solution and 43 nm in the thin film clearly demonstrate the influence of a single atom (**S to Se**) substitution on the optical properties. As a result, the optical band gap decreases from 2.29 eV (**T4BT**) to 2.13 eV (**T4BSe**) (calculated based on absorption onset). The benzothiadiazole derivative is yellow, whereas it is orange-red for **T4BSe**. As observed previously, the decrease in band gap is due to destabilization of the HOMO and stabilization of the LUMO by replacing sulfur with selenium.[21,25,43] Incorporation of selenium in the acceptor unit reduces the aromaticity, which increases the energy of HOMO and reduces the energy of LUMO and hence the band gap.

Fluorescence followed a similar trend as that of their absorption spectra; **T4BT** emits at 575 nm, whereas emission of **T4BSe** red-shifted to 622 nm. Thin film emission maxima remained at the same position in solution for the respective molecules. The nature of the thin film absorption and emission spectra suggests that in solid-state the aggregation phenomenon affects the ground state to a greater extent than the excited state. For both the molecules, we observe large Stokes shift in chloroform solution. The Stokes shift of 0.63 eV was measured

dx.doi.org/10.1021/am506905b | ACS Appl. Mater. Interfaces 2015, 7, 670−681

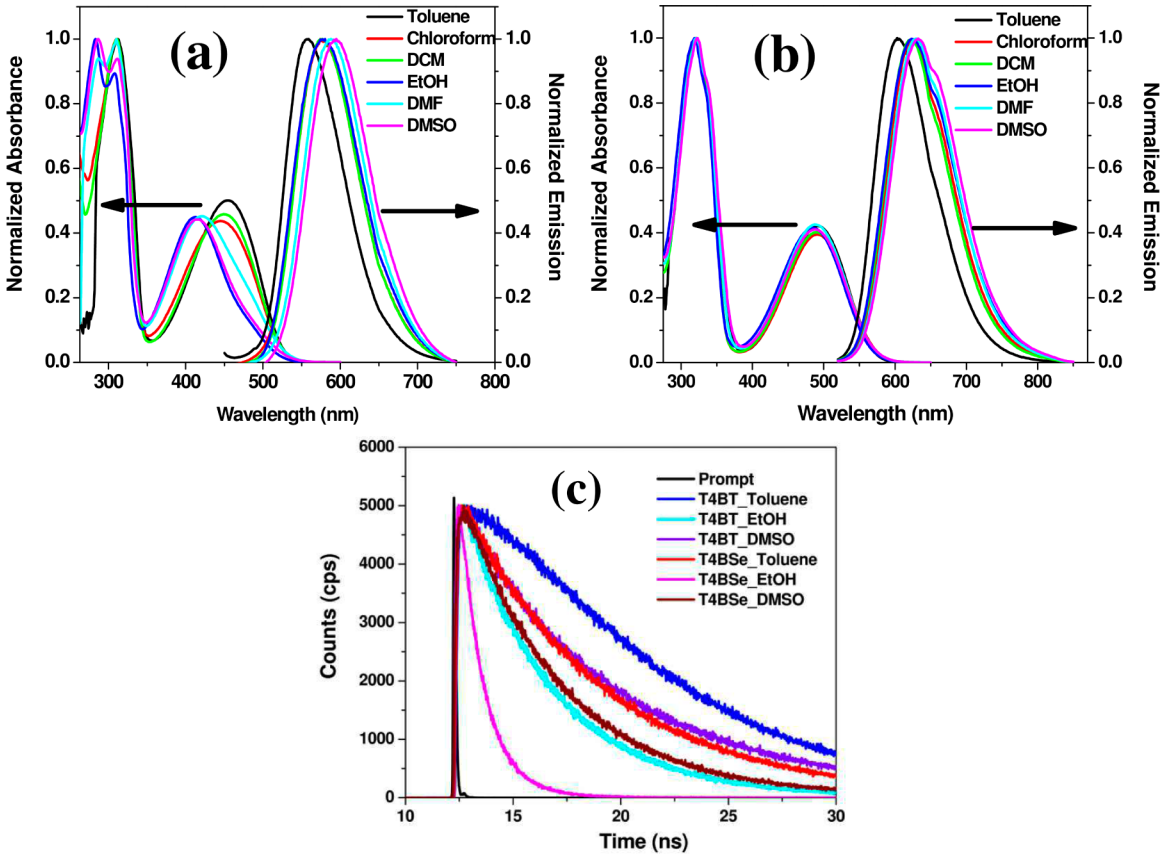

Figure 2. Absorption and emission spectra of (a) **T4BT** and (b) **T4BSe** collected in different polarity solvents at room temperature. (C) shows the fluorescence excited state decay profile for **T4BT** and **T4BSe** in different polarity solvents.

for **T4BT**, whereas 0.53 eV was recorded for **T4BSe**, indicating substantial stabilization of the excited state due to solvation. Similar to our previous observation, the photoluminescence quantum yield (PLQY) reduces from the sulfur to selenium analog because of the heavy atom effect.[44,45] In chloroform solution, **T4BT** exhibited PLQY about 87%, but it drops to 70% for **T4BSe**. The optical properties are summarized in Table 1.

Further, we have performed a solvatochromic study of these two molecules to ascertain the role of the chalcogen atom in governing the optical properties of **T4BT** and **T4BSe.** We have found that with the increase in solvent polarity, **T4BT** showed only a blue shift in its low energy absorption band, but there was no shift in **T4BSe** absorption peak maxima (Figure 2). The position of the $\pi \rightarrow \pi^*$ band remained unchanged for **T4BT** but minor shift and intensification of the specific transition of the $\pi \rightarrow \pi^*$ band were observed by increasing the solvent polarity. The effect of solvent polarity on the charge transfer band of **T4BT** clearly reflects as maxima shifts from 455 to 415 nm from toluene to DMSO. This observation indicates that either **T4BT** has substantial ground state polarity which changes significantly from the ground to the excited state in amplitude or in direction, leading to reorientation of solvent molecules around the chromophores or it forms aggregates in the solvents of a higher dielectric constant and hence shows polarity-dependent absorption spectra. To investigate such behavior, we further recorded temperature-dependent UV–visible absorption spectra of **T4BT** in toluene and DMSO. Temperature-dependent absorption measurement (see Figure S6a in the Supporting Information) in toluene showed that the maxima of low as well as of high-energy band did not shift with increase in temperature and the intensities of the spectra remain the same as a function of temperature. On the contrary, in DMSO, when the temperature increased from 15 to 60 °C, a drastic change in the UV–visible absorption spectra (see Figure S6b in the Supporting Information) was observed. The charge-transfer band red-shifted from 427 to 457 nm with gradual increase in temperature with concomitant increase in the intensity although the $\pi \rightarrow \pi^*$ band did not shift much from 411 nm. This observation explains the origin of the blue shift of the low energy band. **T4BT** molecules tend to aggregate with an increase in the solvent polarity and the aggregation affects mainly the charge transfer band whereas the high-energy band remains unaffected. The intensity enhancement can be ascribed to the increased solubility of **T4BT** with the rise in temperature. In toluene, however, **T4BT** molecules stay in a nonaggregated, solvated state. In the case of **T4BSe**, in different solvents, we did not observe any shift in the maxima of the absorption band, indicating that the polarity of the solvents does not affect its solubility. Because of higher polarizability and the lower electronegativity of selenium compared to sulfur, solubility of **T4BSe** does not change with an increase in the solvent polarity.

Similar to the absorption spectrum, fluorescence spectra were also monitored in solvents of different polarities (same set of solvents used in the UV–visible absorption experiment). Both the molecules showed a bathochromic shift with an increase in solvent polarity, as excited state is more polar in comparison with the ground state. The fluorescence of **T4BT** in toluene exhibited a peak centered at 557 nm when it was excited at 440

dx.doi.org/10.1021/am506905b | ACS Appl. Mater. Interfaces 2015, 7, 670–681

nm, but in DMSO, the peak maxima shifts to 595 nm. In case of **T4BSe**, an increase in the solvent polarity red shifts the fluorescence maxima by 30 nm from toluene to DMSO. From this observation, we can consider that the degree of stabilization attained by the excited state due to an increase in the solvent polarity was comparable for both the molecules. Moreover, a new vibronic feature arises for **T4BSe**, but was not visible in **T4BT** as we move from toluene to DMSO.

The fluorescence lifetime measurement also highlights the influence of a single atom substitution in the molecular semiconductor as we observe drastic changes in the excited-state lifetime of the corresponding species in different solvents (Figure 2c). Three solvents, toluene, ethanol, and DMSO were used to analyze the time-dependent fluorescence measurements. Toluene is a highly nonpolar solvent, whereas DMSO has the highest dielectric constant among the three solvents. On the other side, ethanol is a polar protic solvent with intermediate polarity. Excited-state lifetime values of **T4BT** and **T4BSe** with corresponding amplitude are listed in T1 (see the Supporting Information). In toluene, **T4BT** and **T4BSe** show single-component excited-state decay though lifetime reduced to 6 ns for **T4BSe** from 10 ns of **T4BT**. Biexponential decay is observed for **T4BT** in DMSO, whereas **T4BSe** showed a single exponential decay profile. For **T4BT** in DMSO, the lifetime of two excited-state components are 9 and 5 ns. Lifetime (4.8 ns) of the single excited-state species of **T4BSe** is shorter than both the species of **T4BT** in DMSO. In a similar fashion, we have found that the lifetime of the two excited-state species of **T4BSe** is much shorter than the single component of **T4BT** in ethanol. Because selenium is more electropositive than sulfur, it is expected that the selenium will have stronger interaction with the ethanol molecules, leading to faster decay in protic solvents.

3.2. Theoretical Calculations. Density functional theory (DFT) calculations were performed to determine the optimized geometry of the ground state, electron density distribution and the energy associated with the frontier molecular orbitals. The B3LYP function with 6-31G(d) basis set was employed for the geometry optimization in Gaussian 03 suite program. The optimized geometries and electron density distribution in the HOMO and LUMO of these two benzochalcogenadiazole derivatives are shown in Figure 3. The optimized geometry of **T4BSe** exhibits the trans-orientation of the thiophene rings with respect to each other. But in **T4BT**, thiophene units orient in cis-geometry with the sulfur atom of the thiophene ring facing in opposite direction to the thiadiazole moiety. The donor and the acceptor groups are placed almost in the same plane with small variations in torsional angle. In **T4BT**, the torsions were measured to be 2 and 5°, whereas the torsions are 3 and 14° for **T4BSe**. The electron density distribution in frontier molecular orbitals is similar to both the molecules. In the HOMO, the electron density mainly delocalizes over the two thiophene rings and phenyl ring of the benzochalcogenadiazole unit. But in the LUMO, it localizes only on the benzochalcogenadiazole moiety. The inter-ring C−C bond lengths between the donor and acceptor are similar in both the molecules with 1.46 Å, but the N−X (X = S/Se) distance varies significantly in **T4BSe** from **T4BT**. N−S bond length is 1.64 Å, whereas N−Se bond distance increases to 1.79 Å.

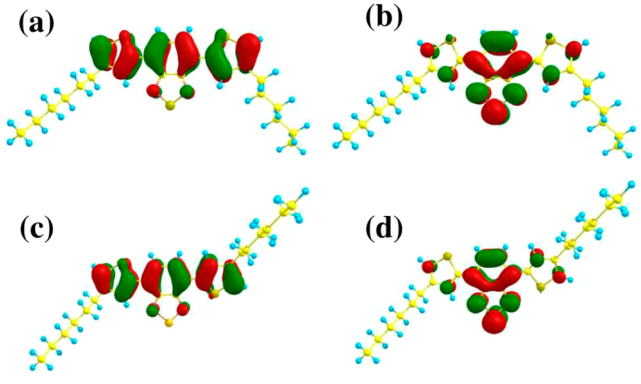

Figure 3. Electron density distribution associated with the energy minimized ground state geometry of the (a, c) HOMO and (b, d) LUMO in (a, b) **T4BT** and (c, d) **T4BSe**.

With the substitution of sulfur by selenium, HOMO has been found to destabilize with concomitant stabilization of LUMO, leading to the decrease in the band gap. HOMO energy level of **T4BT** has been calculated to be −5.24 eV as compared to −5.16 eV of **T4BSe**. The decrease in aromaticity with the selenium inclusion leads to the increase in the HOMO energy level. It can be seen that the electron density resides on a chalcogen atom in the LUMO. Hence, changes in the chalcogen atom directly influence the LUMO energy level of organic semiconductors. In present study, LUMO has been found to stabilize by 0.06 eV from −2.55 eV of **T4BT** to −2.61 eV of **T4BSe**, as a result the band gap is reduced by 0.14 eV by integration of selenium.

3.3. Electrochemical Studies. The redox properties of studied molecules were evaluated by cyclic voltammetry. The HOMO, LUMO, and corresponding band-gaps were calculated from the measured potentials (Figure 4). **T4BT** and **T4BSe**

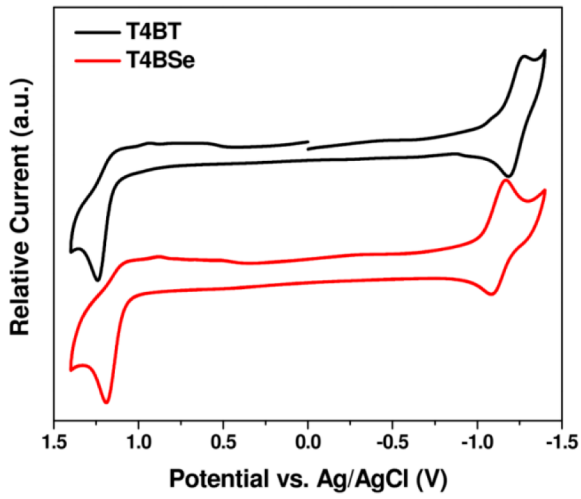

Figure 4. Cyclic voltammograms of **T4BT** and **T4BSe** recorded in chloroform.

exhibit a reversible reduction, but irreversible oxidation peak. The oxidation potential of **T4BSe** decreases to 1.09 V from 1.15 V for **T4BT**. On the other side, incorporation of selenium stabilized the LUMO substantially, which can be seen from their reduction potentials. The reduction potential is reduced by 0.12 V from **T4BT** to **T4BSe**. Calculated energy levels of the HOMO and LUMO of corresponding molecules are given in Table 1. The HOMO energy level increases to −5.49 eV from −5.55 eV and the LUMO energy reduces to −3.39 eV from −3.27 eV in **T4BSe** in comparison with **T4BT**. As a

dx.doi.org/10.1021/am506905b | ACS Appl. Mater. Interfaces 2015, 7, 670−681

result, there was an overall decrease of 0.18 eV by incorporating selenium in the organic framework, achieved by elevating and lowering the energy levels of HOMO and LUMO than that of **T4BT**, respectively. The destabilization of HOMO orbital in **T4BSe** is associated with the lower aromaticity and weaker electron-withdrawing power of the benzoselenadiazole acceptor unit, whereas the stabilization of LUMO has been assigned to the lower electronegativity and ionization potential of selenium.[21]

3.4. Crystal Structure and Packing Diagram. The crystal structure and packing of molecules in a unit cell were studied by single crystal X-ray diffraction measurement. Both the molecules formed fine fiber like single crystals from chloroform/acetone solvent mixture during the slow evaporation method. Both of them grew in the triclinic space group *P*-1 with $z = 2$ with an inversion symmetry with respect to two thiophene groups. The thiophene units show trans-orientation in both the molecules (see Figure S7 in the Supporting Information). The packing of molecules in the unit cell follows a slip-stack pattern where the acceptor group, e.g., benzothiadiazole or benzoselenadiazole appears closer to the donor thiophene unit (Figures 5 and 6). The $\pi-\pi$ stacking distances

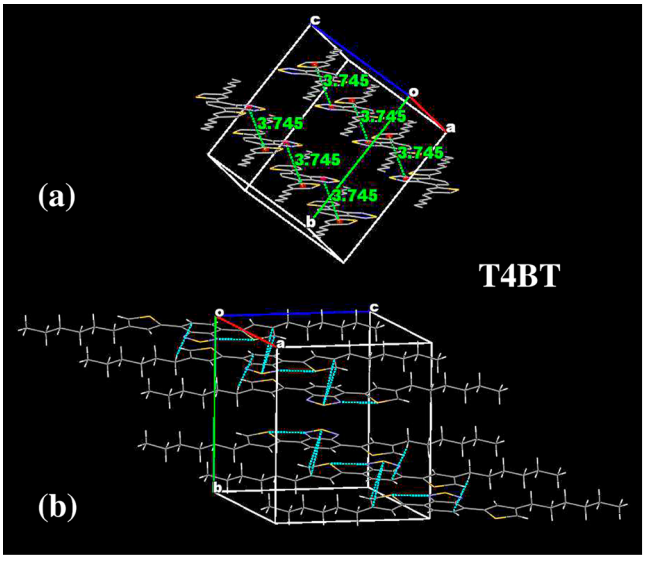

Figure 5. (a) Unit-cell packing diagram and (b) different short noncovalent interactions in **T4BT**.

between the thiophene and benzothiadiazole/benzoselenadiazole in **T4BT** and **T4BSe** have been measured to be 3.74 and 3.95 Å, suggesting stronger $\pi-\pi$ overlap in **T4BT** as compared to **T4BSe**. Both the molecules are almost planar with donor and acceptor groups lying in the same plane. The thiophene units attached to the benzochalcogenadiazole show different torsion in **T4BT** and in **T4BSe**. In **T4BT**, the observed torsion angle is 5 and 9°, whereas torsions of 3 and 10° are observed in **T4BSe**. Different short noncontact interactions, like S···N, C···S, C···H are present in both the molecules. Similar kind of an intramolecular S···N interaction was found to operate between S atom in thiophene and N atom of benzothiadiazole or benzoselenadiazole in both the crystals. The S···N distances were found close to 2.83 and 2.85 Å in **T4BT** and **T4BSe**, respectively.

In both the molecules, the degree of torsions is varied because of the S···N interaction between donor and acceptor

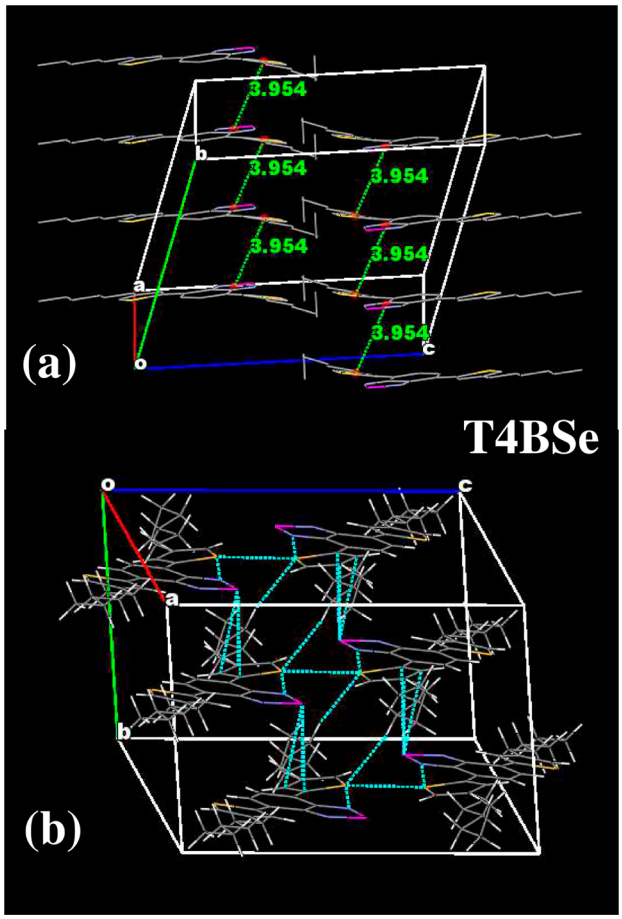

Figure 6. (a) Unit-cell packing diagram and (b) different short noncovalent interactions in **T4BSe**.

groups. Greater torsion of 9 and 10° in **T4BT** and **T4BSe** has been measured between benzochalcogenadiazole and the thiophene ring, which is involved in an intramolecular S···N interaction. On the other side, the donor–acceptor intermolecular interactions are mainly governed by the two C···S and three C···Se weak interactions in **T4BT** and **T4BSe**, respectively. The distances of 3.46 and 3.49 Å are determined between C atoms of thiophene unit and S atom of benzothiadiazole moiety in **T4BT**, whereas those three distances in **T4BSe** are 3.58, 3.54, and 3.52 Å in between the Se and C atom. The S atom of thiophene that interacts with the N atom of selenadiazole unit also involved in S···S interaction with a similar S atom of neighboring **T4BSe** molecule present in a unit cell. This distance is measured to be 3.26 Å. But the same kind of interaction is not observed in **T4BT** because the distance between two similar S atoms is too large to have any kind of noncovalent interaction. Another quite unusual intermolecular C–H···C interaction has been found to operate within very short distances in both the crystals. The hydrogen atom present in the hexyl chain interacts with a carbon atom of the benzene ring of benzochalcogenadiazole in a neighboring molecule with a distance of 2.87 and 2.82 Å in **T4BT** and **T4BSe**, respectively. In **T4BSe**, we also observe a C–H···S interaction between a hydrogen atom of the alkyl chain and S atom of the donor thiophene unit. The hydrogen–sulfur distance was measured to be 2.94 Å. The same kind of interaction is not observed in **T4BT**.

dx.doi.org/10.1021/am506905b | *ACS Appl. Mater. Interfaces* 2015, 7, 670–681

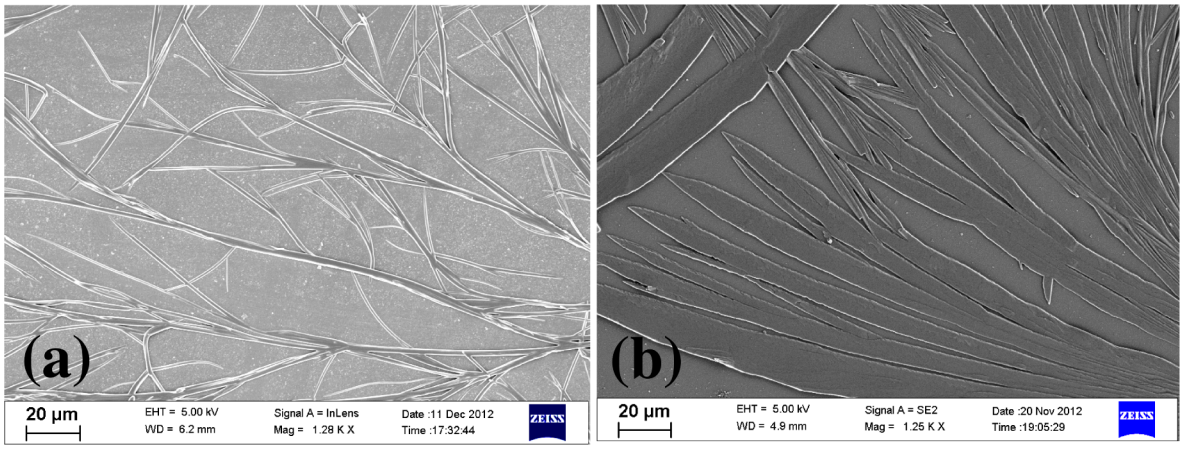

Figure 7. FESEM images of the self-assembled microstructures from (a) **T4BT** and (b) **T4BSe** spin-coated from chloroform/dichlorobenzene solvent mixture (3:1).

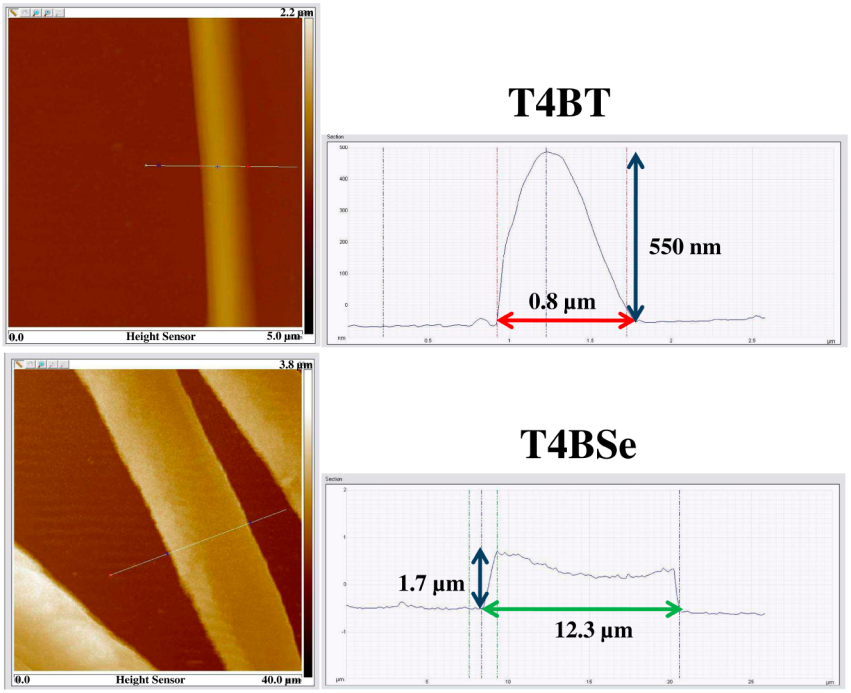

Figure 8. AFM images and corresponding height profile of the self-assembled microstructures from **T4BT** and **T4BSe** on silicon substrate.

3.5. Self-Assembly and Morphological Studies. The self-assembly of **T4BT** and **T4BSe** were further characterized by electron microscopy. We observe self-assembly in the solid state, which leads to the formation of microstructures when drop-casted or spin-coated on common substrates. Figure 7a, b are the FESEM images of **T4BT** and **T4BSe** spin-coated from a chloroform/dichlorobenzene solvent mixture (3:1), respectively. Two different morphologies were observed. **T4BT** showed a fibrillar structure, whereas in the case of **T4BSe**, a flat microribbon-like morphology appeared in both spin-coating and drop-casting method. In all the samples, we observed the growth of the microstructures from some specific points which acted as nucleation centers to grow the microfiber or ribbon depending on the nature of the semiconductors. All these structures were found to be ∼100 μm in length and few micrometers in width. Regardless of the nature of the substrate, we observed similar morphologies. The **T4BSe** microstructure was much wider as compared to the **T4BT** microfibers. This can be attributed to the various intermolecular interactions in **T4BSe**, observed in the single-crystal analysis leading to stronger anisotropic stacking. Nucleation and growth of **T4BT** microfibers is associated with extensive branching. The ribbonlike morphology of **T4BSe** was almost devoid of such branched structure. But, by controlling the solution concentration of **T4BT** during SEM sample preparation, we were able to fabricate unbranched single microfiber up to 300 μm in length.

Morphological evolution of **T4BT** and **T4BSe** in solvents of different polarities was investigated by SEM imaging after drop-casting a film on a silicon wafer. There was a fine correlation between optical properties with the morphological features. The morphology of **T4BSe** did not change with variation in solvent polarities. From toluene to DMSO, the characteristic flat morphological feature remained unperturbed though the microstructures varied in their length, indicating similar packing irrespective of solvent dielectrics (see Figure S8 in the

dx.doi.org/10.1021/am506905b | ACS Appl. Mater. Interfaces 2015, 7, 670−681

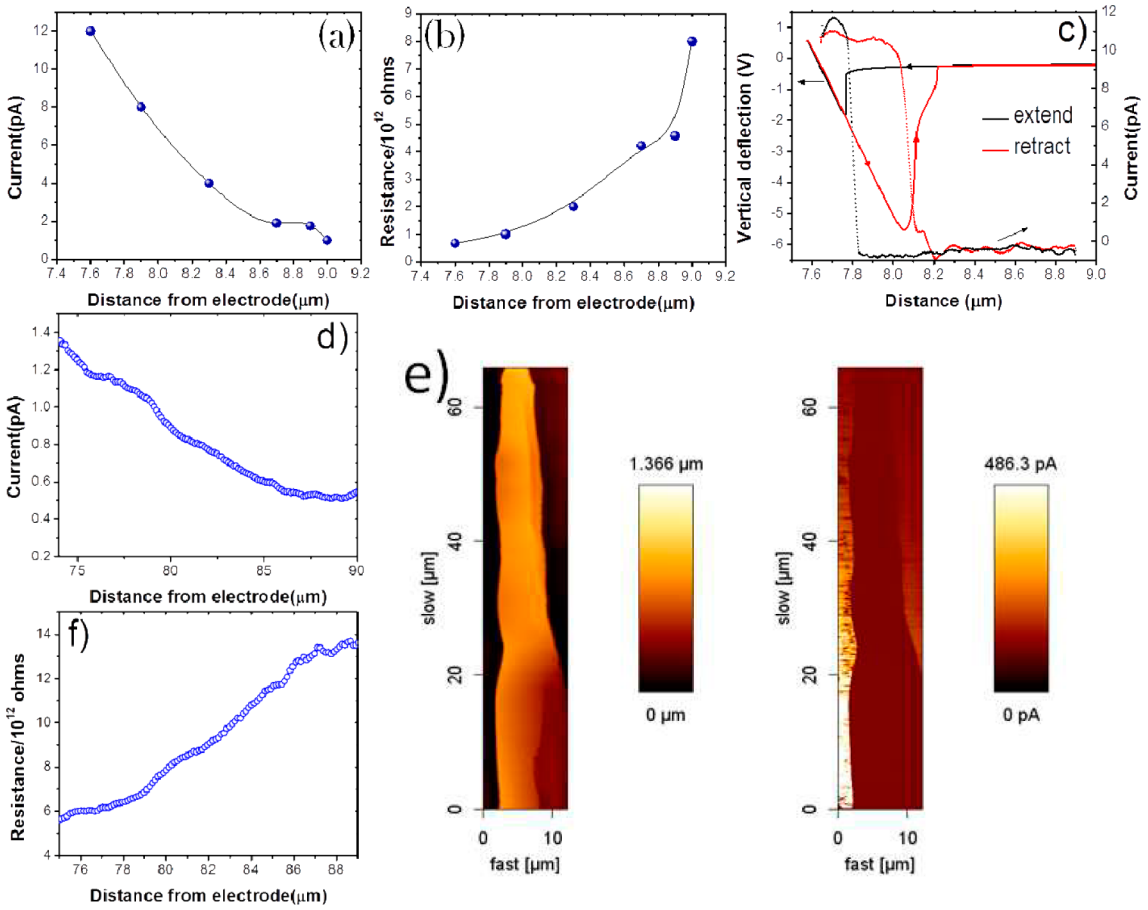

Figure 9. Representative curves showing the typical trend in CP-AFM measurements. (a, d) Current and (b, f) resistance obtained for different distances at the point of contact of tip with the microstructures from (a, b) **T4BT** and (d, f) **T4BSe** in a force scan for a bias of 8 V. (c) Representative force curve along with the current values for one cycle of extend and retract of the AFM cantilever tip. (e) Topography and current image as a function of distance from the gold electrode of **T4BSe** (y-axis is relative). Width of the micro ribbon is 8.48 μm and height is 1.36 μm. The error bar for spatial resolution in the scanning mode is ~2 nm and the current was measured using an amplifier where the background noise level is ~0.3 pA. A number of fibers for which the contact resistance was <1 kΩ (channel resistance is of the order of MΩ) were scanned for each material type, and it was ensured that the loading force and voltage bias were held constant for all the scans.

Supporting Information). On the contrary, for **T4BT** there was a significant turnaround in morphology when the solvent polarity was gradually increased (see Figure S9 in the Supporting Information). In a highly nonpolar solvent like toluene, it formed long-branched fibers, which remained the same in chloroform. But in DCM, these fibers could not grow longer as DCM evaporates very fast limiting their length. In ethanol, sharp needlelike structures were observed. Clear differences were further visible when samples were prepared from two highly polar solvents like DMF and DMSO. In these two solvents, the morphology flattened from the spherical microfiber and they were shortened in their length. The decrease in length and the reduction in branching can be attributed to the higher dielectric constant of these polar solvents, which reduced the intermolecular interactions. We believe that becaues of low solubility in highly polar solvents, **T4BT** remained as aggregates and while the solvent evaporates the molecules precipitate out faster as smaller crystallites without any fibrillar morphology. On the contrary, in solvents of low polarity, the molecules dissolve well and when the solvent evaporates the molecules come close to each other and self-assemble as fibers with different length-scales depending on the rate of solvent evaporation. Thus, the variation in aggregation is directly reflected in their absorption spectra, as observed previously in the solvatochromic studies. Because of the change in morphology, conjugation length varies, resulting in solvatochromism in the absorption spectrum of **T4BT**. But **T4BSe** was found to be more soluble in all the solvents because of the electropositive nature of selenium and hence **T4BSe** does not show any solubility dependent aggregation behavior. Thus, our microscopic observation correlates the optical characterization to establish the solvent-dependent aggregation phenomenon in this class of molecular semiconductors.

From AFM images and corresponding height profiles (Figure 8), it is distinctly evident that a single atom variation provides drastic changes in molecular packing leading to the morphological variation in organic semiconductors. **T4BT** packs in a tubular fashion from toluene resulting in microfiber formation with a diameter of a few hundred of nanometers. The height of such microfibers was measured to be 500 nm while the width was around 1−1.5 μm. On the contrary, **T4BSe** forms ribbonlike flat morphology with the ribbon width around 8−12 μm and height of ~2 μm, which implies stronger packing in the selenium incorporated molecular semiconductor as observed in single-crystal X-ray analysis.

3.6. Thermal Properties. Thermal characteristics were evaluated by TGA and DSC analysis. TGA (see Figure S10 in the Supporting Information) indicates higher thermal stability

dx.doi.org/10.1021/am506905b | ACS Appl. Mater. Interfaces 2015, 7, 670−681

of **T4BSe** as compared to **T4BT**. The TGA plot suggests that the **T4BT** has lesser decomposition temperature as compared to **T4BSe** and completely decomposes before 400 °C but **T4BSe** does not. Hence, integration of selenium in place of sulfur provides superior thermal stability as clearly reflected in their TGA analysis.

DSC experiment was further performed to monitor the thermal behavior of these two materials during heating and cooling processes (see Figure S11a in the Supporting Information). **T4BT** melts at a lower temperature (55 °C) (29 kJ/mol) as compared to the **T4BSe** (72 °C) (18.4 kJ/mol), indicative of stronger intermolecular interaction in **T4BSe** than in **T4BT**. The interesting observation in the DSC curve for **T4BSe** is the presence of a dual thermal transition in the heating and cooling cycles. The first transition appears at 47 °C (5.1 kJ/mol) and second at 72 °C. From polarizing optical microscopic (POM) studies, we observed that at the first transition a liquid crystalline phase (nematic) appears (see Figure S11b in the Supporting Information) and exists until it melts completely into an isotropic phase at 75 °C. In the cooling cycle, these two peaks overlap with each other with a substantial hysteresis. The strong intermolecular interaction in **T4BSe** observed in single-crystal X-ray analysis is believed to be responsible for liquid crystalline behavior.

3.7. Conductivity Studies. Conducting AFM technique was used to monitor charge transport pathways along the long axis of the fiber between a gold coated AFM cantilever and a conducting substrate and relate it to the topography image. The gold electrode was patterned on glass coverslips to carry out electrical transport measurements on an isolated microfiber or ribbon. It was possible to lay the microfiber or ribbon on the gold region of the electrode with a fraction extending outside on the substrate. This enabled us to perform a distance dependent current scan to observe the lifetime of injected charges as the tip is moved farther away from the gold electrode. This is quantitatively depicted in Figure 9 for an 8 V bias applied to the gold electrode. The current reduces linearly as the distance between the AFM cantilever tip is increased from the gold electrode confirming the origin of resistance. Beyond 90 μm, current is negligible and cannot be resolved. The resistance measured is the total resistance R_{tot} which can be decomposed as follows

$$R_{tot} \approx R_{AFMtip} + R_{tip/sample} + R_{sample} + R_{back}$$

R_{AFMtip} is the intrinsic resistance of the AFM tip. This can be neglected since it is of the order of 300 Ω as obtained from the cantilever datasheet. R_{back} is the back contact resistance between the gold electrode and the semiconductor which can also be neglected in view of the large area of contact. R_{sample} is the intrinsic resistance of microstructure equal to $\rho l/S$ where ρ, l, and S are the resistivity, the length and sectional area of the fiber/ribbon, respectively. $R_{tip/sample}$ refers to the contact resistance involving the AFM tip and the semiconducting sample. This was minimized by increasing the applied force (set point) during a contact, using a high voltage bias (8 V) and slow scan speeds to reduce frictional resistance which arises due to high forces. All the above-mentioned parameters were maintained for both the samples for ease of comparison. The conductivity (σ) of the sample can be obtained from the graph above by $\sigma = 1/(A\Delta R/\Delta l)$ where, A is the cross-sectional area of the ribbon and $(\Delta R/\Delta l)$ is the slope obtained from the resistance plot. The conductivity was estimated from regions exhibiting linear $R(L)$. It should be mentioned that the accurate estimate of σ presumes exact knowledge of the cross-sectional geometry and assumption of the uniformity in shape across the entire length of the ribbon or the fiber. For a ribbon of width 8.48 μm and height 1.97 μm, the conductivity is $\sim 5.6 \times 10^{-7} \pm$ 10% S/m. Similarly, by performing an AFM scan on the **T4BT** fiber at a bias of 8 V, we obtain a spatial response as shown in Figure 9 a, b. Figure 9e shows the topography and current images of **T4BSe**. A current map could not be obtained for **T4BT** as the adhesive force between the glass substrate and the fiber was weak, which led to breakage of the fiber during the scan. However, multiple force scans at different points along the fiber were performed and the current obtained at the point of contact was plotted as a function of distance as shown in Figure 9a. Figure 9c shows a representative force scan with simultaneous current measurement at a point on an isolated **T4BT** fiber. The conductivity of **T4BT** can be then obtained with the set of assumptions as mentioned above. For a fiber of width 3.2 μm and height of 594 nm, the conductivity obtained is $\sim 1.4 \times 10^{-6}$ S/m (for a rectangular cross-section), $\sigma = 1.7 \times 10^{-6}$ S/m (for an elliptical cross-section) with an uncertainty factor of ±10%. This estimate of σ in **T4BT** fibers appears to be marginally higher than **T4BSe**.

From the CP-AFM in Figure 9e and the current/distance graphs (Figure 9f), it is clear that the current along the fiber reduced as the cantilever was moved farther from the gold substrate. Indeed, this confirms that the injected charge is transported along the axis of the fiber and indicates that molecular packing plays an important role in determining conduction pathways in organic semiconductors. While comparing two materials with different molecular packing, CP-AFM is a useful technique for electrical characterization at the microscopic scale. This enabled us to obtain conductivity estimates for both the materials, which relates very well with the comparison of molecular packing as explained by the characterization techniques mentioned above. Some important conclusions relating the current values as obtained from CP-AFM and the supramolecular ordering in **T4BT** and **T4BSe** are explained below. First, the observation of a variation in the current in the planar configuration is a proof of $\pi-\pi$ stacking of the molecules along the long axis of the fiber/ribbon. However, the short, noncovalent, intermolecular interactions in these two molecules are different which affect their supramolecular stacking. Crystal structure and packing data yield a larger intermolecular $\pi-\pi$ stacking distance (3.95 Å) between the donor and acceptor units in **T4BSe** as compared to 3.74 Å in **T4BT**.

Similarly, C···S intermolecular distance (3.48 Å) in **T4BT** is shorter as compared to the C···Se intermolecular distance (3.58 Å) in **T4BSe**. Second, the shift in absorption maxima in a charge transfer band from solution to thin film in **T4BT** and **T4BSe** is 45 and 19 nm, respectively. This shows a greater degree of aggregation in **T4BT** as compared to **T4BSe**. The difference in torsional angles of the two thiophene moieties is larger in **T4BSe** (7°) as compared to **T4BT** (4°). This could point to the fact that stacking in **T4BT** could lead to a more planar supramolecular structure as compared to **T4BSe**. It should be noted that besides these factors, contribution of defects at the bulk, macroscopic level can significantly alter the structure−property correlation. The energetics and the distribution of the trap states in the two model systems can further elucidate the trends in the electrical measurements.

The studied molecules show extraordinary luminescence at their respective band edge which enabled us to perform

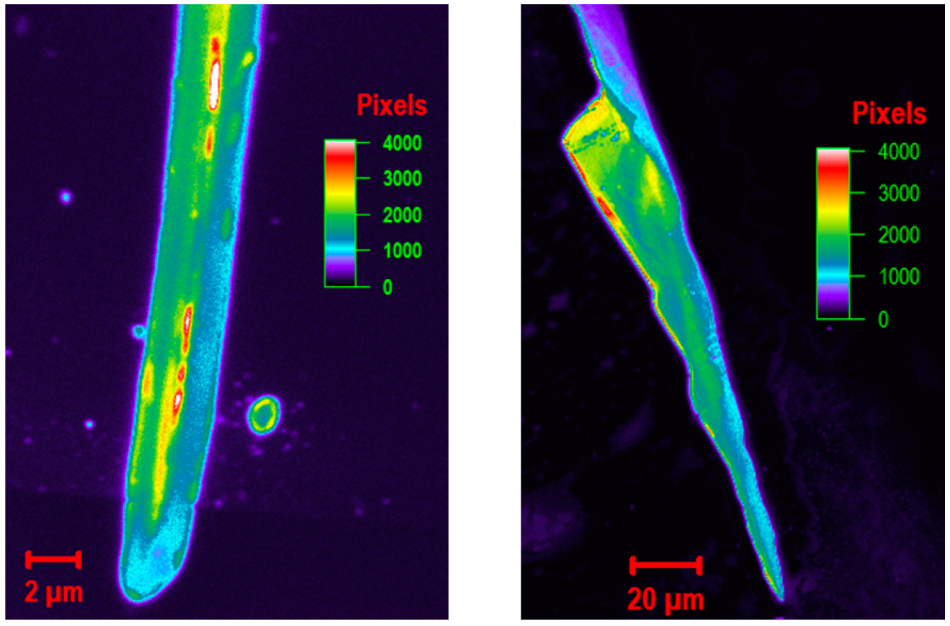

Figure 10. Confocal images (0.1 × 0.1 mm) of (a) **T4BSe** and (b) **T4BT** microstructures in false color. The color palette shows the intensity amplitude of luminescence in pixels.

confocal microscopy simultaneously with CP-AFM on the microstructures to observe any qualitative changes between the two molecules. Figure 10 shows a representative confocal scan for each molecule type (in false color). The intensity of luminescence is not uniform in both the microstructures. Although **T4BSe** shows comparatively higher intensities at the edges of the microstructure, **T4BT** is more luminescent at the center. This reveals that the stacking of chromophores is not similar in the two molecules, but no quantitative conclusions can be made because of their varied microstructure size. Unit-cell packing data shows that both grow in the triclinic space group *P*-1 with $z = 2$ but different nature of molecular interactions leads to the different density of packing. However, because the melting points of both the compounds were very low, analysis of the self-assembled stacking pattern through transmission electron microscopy was not successful.

4. CONCLUSION

In conclusion, we have investigated in detail the structure–property relationship in organic semiconductors with respect to their electrical and optical properties by comparing two D-A-D molecules differing only by a chalcogen atom. These two molecules, **T4BT** and **T4BSe** show substantial variation in their properties with the mere substitution of sulfur with a selenium atom at the acceptor unit of the semiconductors. Introducing selenium caused a decrease in the band gap of **T4BSe** as compared to **T4BT** with concomitant changes in optical properties. Inclusion of selenium in the acceptor moiety reduces the oscillator strength leading to the decrease in the absorption coefficient of selenium derivative. Single-crystal X-ray diffraction clearly reflects stronger intermolecular interactions in the selenium analog in comparison with its sulfur-based counterpart. Heteroatom substitution also led to different molecular packing and aggregation behavior in the two molecules. This was further reflected in their microscale morphology with **T4BT** forming microfibers and **T4BSe** forming microribbons. Conductivity measurements performed by **CP-AFM** on single microstructure gave a further insight into the structure–property correlations of these two molecules. The conductivity of **T4BT** was marginally higher than **T4BSe**, possibly because of smaller π–π stacking distance, higher degree of aggregation, and higher degree of planarity of the molecule and a possible difference in the trap distribution and energetics.

■ ASSOCIATED CONTENT

Ⓢ Supporting Information

Detailed synthesis, additional spectra, microscope images, and fluorescence lifetime. This material is available free of charge via the Internet at http://pubs.acs.org.

■ AUTHOR INFORMATION

Corresponding Author

*E-mail: satish@sscu.iisc.ernet.in. Tel: +91-80- 22932651. Fax: +91-80-23601310.

Notes

The authors declare no competing financial interest.

■ ACKNOWLEDGMENTS

We thank Ms. Anitha A. and Dr. Raja Bhaskar Kanth for helping us in synthesis and theoretical analysis, respectively. J.D. greatly acknowledges the Council of Scientific and Industrial Research (CSIR) for a senior research fellowship (SRF). K.S. acknowledges Ashar A. Z. for his help with the C-AFM measurements. The authors also acknowledge SID and CeNSE (IISc.) for providing the characterization facilities. The authors thank the Ministry of Communication and Information Technology under a grant for the Centre of Excellence in Nanoelectronics, Phase II.

■ REFERENCES

(1) Katz, H. E. Recent Advances in Semiconductor Performance and Printing Processes for Organic Transistor-Based Electronics. *Chem. Mater.* **2004**, *16*, 4748–4756.

(2) Gunes, S.; Neugebauer, H.; Sariciftci, N. S. Conjugated Polymer-Based Organic Solar Cells. *Chem. Rev.* **2007**, *107*, 1324–1338.

(3) Hains, A. W.; Liang, Z. Q.; Woodhouse, M. A.; Gregg, B. A. Molecular Semiconductors in Organic Photovoltaic Cells. *Chem. Rev.* **2010**, *110*, 6689−6735.
(4) Murphy, A. R.; Frechet, J. M. J. Organic Semiconducting Oligomers for Use in Thin Film Transistors. *Chem. Rev.* **2007**, *107*, 1066−1096.
(5) Li, Y. F. Molecular Design of Photovoltaic Materials for Polymer Solar Cells: Toward Suitable Electronic Energy Levels and Broad Absorption. *Acc. Chem. Res.* **2012**, *45*, 723−733.
(6) Liang, Y.; Yu, L. A New Class of Semiconducting Polymers for Bulk Heterojunction Solar Cells with Exceptionally High Performance. *Acc. Chem. Res.* **2010**, *43*, 1227−1236.
(7) Wang, C. L.; Dong, H. L.; Hu, W. P.; Liu, Y. Q.; Zhu, D. B. Semiconducting pi-Conjugated Systems in Field-Effect Transistors: A Material Odyssey of Organic Electronics. *Chem. Rev.* **2012**, *112*, 2208−2267.
(8) Cheng, Y. J.; Yang, S. H.; Hsu, C. S. Synthesis of Conjugated Polymers for Organic Solar Cell Applications. *Chem. Rev.* **2009**, *109*, 5868−5923.
(9) Coropceanu, V.; Cornil, J.; da Silva Filho, D. A.; Olivier, Y.; Silbey, R.; Bredas, J.-L. Charge Transport in Organic Semiconductors. *Chem. Rev.* **2007**, *107*, 926−952.
(10) Kanimozhi, C.; Yaacobi-Gross, N.; Chou, K. W.; Amassian, A.; Anthopoulos, T. D.; Patil, S. Diketopyrrolopyrrole-Diketopyrrolopyrrole-Based Conjugated Copolymer for High-Mobility Organic Field-Effect Transistors. *J. Am. Chem. Soc.* **2012**, *134*, 16532−16535.
(11) Kang, I.; Yun, H.-J.; Chung, D. S.; Kwon, S.-K.; Kim, Y.-H. Record High Hole Mobility in Polymer Semiconductors via Side-Chain Engineering. *J. Am. Chem. Soc.* **2013**, *135*, 14896−14899.
(12) Chen, Z. Y.; Lee, M. J.; Ashraf, R. S.; Gu, Y.; Albert-Seifried, S.; Nielsen, M. M.; Schroeder, B.; Anthopoulos, T. D.; Heeney, M.; McCulloch, I.; Sirringhaus, H. High-Performance Ambipolar Diketopyrrolopyrrole-Thieno[3,2-b]thiophene Copolymer Field-Effect Transistors with Balanced Hole and Electron Mobilities. *Adv. Mater.* **2012**, *24*, 647−652.
(13) Shin, W.; Yasuda, T.; Watanabe, G.; Yang, Y. S.; Adachi, C. Self-Organizing Mesomorphic Diketopyrrolopyrrole Derivatives for Efficient Solution-Processed Organic Solar Cells. *Chem. Mater.* **2013**, *25*, 2549−2556.
(14) Viterisi, A.; Gispert-Guirado, F.; Ryan, J. W.; Palomares, E. Formation of Highly Crystalline and Texturized Donor Domains in DPP(TBFu)(2):PC71BM SM-BHJ Devices via Solvent Vapour Annealing: Implications for Device Function. *J. Mater. Chem.* **2012**, *22*, 15175−15182.
(15) Li, W.; Hendriks, K. H.; Furlan, A.; Roelofs, W. S. C.; Wienk, M. M.; Janssen, R. A. J. Universal Correlation between Fibril Width and Quantum Efficiency in Diketopyrrolopyrrole-Based Polymer Solar Cells. *J. Am. Chem. Soc.* **2013**, *135*, 18942−18948.
(16) Miao, Q.; Lefenfeld, M.; Nguyen, T. Q.; Siegrist, T.; Kloc, C.; Nuckolls, C. Self-Assembly and Electronics of Dipolar Linear Acenes. *Adv. Mater.* **2005**, *17*, 407−412.
(17) Yan, Y.; Zhao, Y. S. Organic Nanophotonics: from Controllable Assembly of Functional Molecules to Low-Dimensional Materials with Desired Photonic Properties. *Chem. Soc. Rev.* **2014**, *43*, 4325−4340.
(18) Kaake, L. G.; Barbara, P. F.; Zhu, X. Y. Intrinsic Charge Trapping in Organic and Polymeric Semiconductors: A Physical Chemistry Perspective. *J. Phys. Chem. Lett.* **2010**, *1*, 628−635.
(19) Tsao, H. N.; Cho, D.; Andreasen, J. W.; Rouhanipour, A.; Breiby, D. W.; Pisula, W.; Muellen, K. The Influence of Morphology on High-Performance Polymer Field-Effect Transistors. *Adv. Mater.* **2009**, *21*, 209−212.
(20) Mativetsky, J. M.; Kastler, M.; Savage, R. C.; Gentilini, D.; Palma, M.; Pisula, W.; Muellen, K.; Samori, P. Self-Assembly of a Donor-Acceptor Dyad Across Multiple Length Scales: Functional Architectures for Organic Electronics. *Adv. Funct. Mater.* **2009**, *19*, 2486−2494.
(21) Gibson, G. L.; McCormick, T. M.; Seferos, D. S. Atomistic Band Gap Engineering in Donor−Acceptor Polymers. *J. Am. Chem. Soc.* **2011**, *134*, 539−547.
(22) Hollinger, J.; DiCarmine, P. M.; Karl, D.; Seferos, D. S. Heterocycle-Induced Phase Separation in Conjugated Polymers. *Macromolecules* **2012**, *45*, 3772−3778.
(23) Perepichka, I. F.; Perepichka, D. F. *Handbook of Thiophene-Based Materials: Applications in Organic Electronics and Photonics*; John Wiley & Sons: Chichester, U.K., 2009.
(24) Kang, I.; An, T. K.; Hong, J. A.; Yun, H. J.; Kim, R.; Chung, D. S.; Park, C. E.; Kim, Y. H.; Kwon, S. K. Effect of Selenophene in a DPP Copolymer Incorporating a Vinyl Group for High-Performance Organic Field-Effect Transistors. *Adv. Mater.* **2013**, *25*, 524−528.
(25) Kronemeijer, A. J.; Gili, E.; Shahid, M.; Rivnay, J.; Salleo, A.; Heeney, M.; Sirringhaus, H. A Selenophene-Based Low-Bandgap Donor-Acceptor Polymer Leading to Fast Ambipolar Logic. *Adv. Mater.* **2012**, *24*, 1558−1565.
(26) Lee, J.; Han, A. R.; Kim, J.; Kim, Y.; Oh, J. H.; Yang, C. Solution-Processable Ambipolar Diketopyrrolopyrrole-Selenophene Polymer with Unprecedentedly High Hole and Electron Mobilities. *J. Am. Chem. Soc.* **2012**, *134*, 20713−20721.
(27) Bedi, A.; Senanayak, S. P.; Narayan, K. S.; Zade, S. S. Synthesis of Solution-Processable Poly(cyclopenta[c]selenylvinylene) and Its Charge Transport Properties: Comparative Study with the Thiophene Analogue. *Macromolecules* **2013**, *46*, 5943−5950.
(28) Zade, S. S.; Zamoshchik, N.; Bendikov, M. Oligo- and Polyselenophenes: A Theoretical Study. *Chem.- Eur. J.* **2009**, *15*, 8613−8624.
(29) Patra, A.; Bendikov, M. Polyselenophenes. *J. Mater. Chem.* **2010**, *20*, 422−433.
(30) Gao, D.; Hollinger, J.; Seferos, D. S. Selenophene-Thiophene Block Copolymer Solar Cells with Thermostable Nanostructures. *ACS Nano* **2012**, *6*, 7114−7121.
(31) Chen, Z. Y.; Lemke, H.; Albert-Seifried, S.; Caironi, M.; Nielsen, M. M.; Heeney, M.; Zhang, W. M.; McCulloch, I.; Sirringhaus, H. High Mobility Ambipolar Charge Transport in Polyselenophene Conjugated Polymers. *Adv. Mater.* **2010**, *22*, 2371−2375.
(32) Heeney, M.; Zhang, W.; Crouch, D. J.; Chabinyc, M. L.; Gordeyev, S.; Hamilton, R.; Higgins, S. J.; McCulloch, I.; Skabara, P. J.; Sparrowe, D.; Tierney, S. Regioregular Poly(3-hexyl) Selenophene: a Low Band Gap Organic Hole Transporting Polymer. *Chem. Commun.* **2007**, 5061−5063.
(33) Gidron, O.; Varsano, N.; Shimon, L. J. W.; Leitus, G.; Bendikov, M. Study of a Bifuran vs. Bithiophene Unit for the Rational Design of pi-Conjugated Systems. What Have We Learned? *Chem. Commun.* **2013**, *49*, 6256−6258.
(34) Beaujuge, P. M.; Amb, C. M.; Reynolds, J. R. Spectral Engineering in pi-Conjugated Polymers with Intramolecular Donor-Acceptor Interactions. *Acc. Chem. Res.* **2010**, *43*, 1396−1407.
(35) Zhang, Q. T.; Tour, J. M. Alternating Donor/Acceptor Repeat Units in Polythiophenes. Intramolecular Charge Transfer for Reducing Band Gaps in Fully Substituted Conjugated Polymers. *J. Am. Chem. Soc.* **1998**, *120*, 5355−5362.
(36) Havinga, E. E.; Tenhoeve, W.; Wynberg, H. A New Class of Small Band-Gap Organic Polymer Conductors. *Polym. Bull.* **1992**, *29*, 119−126.
(37) Yang, R. Q.; Tian, R. Y.; Yan, J. G.; Zhang, Y.; Yang, J.; Hou, Q.; Yang, W.; Zhang, C.; Cao, Y. Deep-Red Electroluminescent Polymers: Synthesis and Characterization of New Low-Band-Gap Conjugated Copolymers for Light-Emitting Diodes and Photovoltaic Devices. *Macromolecules* **2005**, *38*, 244−253.
(38) Pati, P. B.; Zade, S. S. MLCT based colorimetric probe for iron having D−A−D type architecture of benzo[2,1,3]thiadiazole acceptor and thiophene donor with azomethine pendant arm. *Inorg. Chem. Commun.* **2014**, *39*, 114−118.
(39) Padhi, H.; Huang, J.-H.; Sahu, D.; Patra, D.; Kekuda, D.; Chu, C.-W.; Lin, H.-C. Synthesis and Applications of Low-Bandgap Conjugated Polymers Containing Phenothiazine Donor and Various Benzodiazole Acceptors for Polymer Solar Cells. *J. Polym. Sci., Part A: Polym. Chem.* **2010**, *48*, 4823−4834.
(40) Helgesen, M.; Gevorgyan, S. A.; Krebs, F. C.; Janssen, R. A. J. Substituted 2,1,3-Benzothiadiazole- And Thiophene-Based Polymers

for Solar Cells - Introducing a New Thermocleavable Precursor. *Chem. Mater.* **2009**, *21*, 2669−2675.
(41) Wen, S.; Pei, J.; Li, P.; Zhou, Y.; Cheng, W.; Dong, Q.; Li, Z.; Tian, W. Synthesis and Photovoltaic Properties of Low-Bandgap 4,7-Dithien-2-yl-2,1,3-Benzothiadiazole-Based Poly-(heteroarylenevinylene)s. *J. Polym. Sci., Part A: Polym. Chem.* **2011**, *49*, 2715−2724.
(42) Zhou, W.; Shen, P.; Zhao, B.; Ziang, P.; Deng, L.; Tan, S. Low Band Gap Copolymers Consisting of Porphyrins, Thiophenes, and 2,1,3-Benzothiadiazole Moieties for Bulk Heterojunction Solar Cells. *J. Polym. Sci., Part A: Polym. Chem.* **2011**, *49*, 2685−2692.
(43) Villar, H. O.; Otto, P.; Dupuis, M.; Ladik, J. Ab-Initio and Electron Correlation Corrected Energy-Band Structure of Polymeric 5-Membered Heterocycles. *Synth. Met.* **1993**, *59*, 97−110.
(44) Pensack, R. D.; Song, Y.; McCormick, T. M.; Jahnke, A. A.; Hollinger, J.; Seferos, D. S.; Scholes, G. D. Evidence for the Rapid Conversion of Primary Photoexcitations to Triplet States in Seleno- and Telluro- Analogues of Poly(3-hexylthiophene). *J. Phys. Chem. B* **2014**, *118*, 2589−2597.
(45) Yang, R. Q.; Tian, R. Y.; Hou, Q.; Yong, Z.; Li, Y. F.; Wei, Y.; Chi, Z.; Yong, C. Light-Emitting Copolymers Based on Fluorene and Selenophene-Comparative Studies with its Sulfur Analogue: Poly-(fluorene-co-thiophene). *J. Polym. Sci., Part A: Polym. Chem.* **2005**, *43*, 823−836.